# Advanced near-infrared-driven photocatalyst: Fabrication, characterization, and photocatalytic performance of β-NaYF$_4$:Yb$^{3+}$,Tm$^{3+}$@TiO$_2$ core@shell microcrystals

Dong-Xing Xu [a,b], Zheng-Wei Lian [a,b], Ming-Lai Fu [a,*], Baoling Yuan [c,**], Jian-Wen Shi [a], Hao-Jie Cui [a]

[a] Key Laboratory of Urban Environment and Health, Institute of Urban Environment, Chinese Academy of Sciences, No. 1799, Jimei Road, Xiamen, Fujian 361021, China
[b] College of Civil Engineering, Fuzhou University, Fuzhou 350108, China
[c] College of Civil Engineering, Huaqiao University, No. 668, Jimei Road, Xiamen, Fujian 361020, China

## A R T I C L E   I N F O

## A B S T R A C T

The β-NaYF$_4$:Yb$^{3+}$,Tm$^{3+}$@TiO$_2$ core@shell photocatalyst has been successfully fabricated by a simply hydrothermal method followed by hydrolysis of titanium isopropoxide (TTIP) with polyvinylpyrrolidone K-30 (PVP) as the coupling agent. The advanced near-infrared-driven photocatalyst was characterized by X-ray diffraction, scanning electron microscopy, transmission electron microscopy, fluorescence spectrometer and UV–vis–NIR diffuse reflectance spectroscopy. It is found that β-NaYF$_4$:Yb$^{3+}$,Tm$^{3+}$@TiO$_2$ core@shell photocatalyst consists of uniform hexagonal phase NaYF$_4$ microcrystals rods and anatase TiO$_2$ shells, and the β-NaYF$_4$:Yb$^{3+}$,Tm$^{3+}$@TiO$_2$ exhibits strong near-infrared light absorption and the energy transfers from β-NaYF$_4$:Yb$^{3+}$,Tm$^{3+}$ to TiO$_2$ is confirmed. The photocatalytic activities of the catalysts were evaluated by the discoloration of Methylene Blue, Methyl Orange and Rhodamine B under the irradiation of 980 nm laser. The results suggest that β-NaYF$_4$:Yb$^{3+}$,Tm$^{3+}$@TiO$_2$ core@shell composite is an advanced near-infrared-driven photocatalyst. Moreover the NIR-driven photocatalyst shows good stability for photocatalytic decoloration of dye in the recycled tests. This study suggests a promising system to utilize the NIR energy of sunlight for photochemical and photoelectrical applications based on TiO$_2$, which will contribute to the utilization of solar energy in the future.

## 1. Introduction

Energy shortages and environmental pollution, associated with the development of science and technology, are the serious problems nowadays encountered by mankind all over the world [1]. It is well known that the environmental quality has deteriorated mostly due to the burning of fossil fuels [2]. Therefore, toward addressing these critical challenges, it is urgent to develop efficient pollution-free technologies for pollution control and producing renewable clean energy to ensure a sustainable society. Solar energy has been widely regarded as one of the most promising renewable energy sources in the world since it is a free, non-polluting, inexhaustible resource and a domestic energy source. Accordingly, photocatalytic technology based on semiconductor has been constantly recognized as a promising green route for application in controlling pollutant and producing energy, such as environmental remediation [3] and hydrogen production [4], because of its ability to utilize the energy of natural sunlight. Among various photocatalysts reported so far, titanium dioxide (TiO$_2$) is undoubtedly the most widely used photocatalyst due to its high stability, low cost and safety toward both human and environment [5–7]. Unfortunately, TiO$_2$ can only be activated by high-energy ultraviolet (UV) light due to its wide band gap (3.0–3.2 eV). It was well documented that the solar spectra reaching Earth's surface compose of UV (290–400 nm), visible (400–760 nm) and infrared (IR) radiation (760–3000 nm), in which the corresponding solar energy is 6.8% in the UV range, 38.9% in the visible range and about 54.3% in the IR spectral range [8]. In the past decades, in order to achieve the efficient photocatalysis of TiO$_2$-based materials under irradiation of solar light, various methods have been explored to arouse the visible-light response of TiO$_2$. Among these, metal and non-metal doping [9–13], dye sensitizing [14], or coupling with a narrow band gap semiconductor with a more negative conduction band level [15] have been confirmed to be viable ways to allow the extension of light absorption

* Corresponding author. Tel.: +86 592 6190762; fax: +86 592 6190977.
** Corresponding author. Tel: +86 18906015873; fax: +86 592 6162698.
  E-mail addresses: mlfu@iue.ac.cn, fuminglai@gmail.com (M.-L. Fu),
blyuan@hqu.edu.cn (B. Yuan).

edge. In this way, the activities of $TiO_2$-based photocatalysts can be improved to some extent. In order to improve the catalytic efficiencies of $TiO_2$-based photocatalysts to the highest degree, it is urgent to design and fabricate the near-infrared (NIR) light active photocatalysts. However, to the best of our knowledge, so far the reported examples of modified $TiO_2$ composites, which can be activated by NIR light, mostly are based on dye and quantum dots and are very limited [16–19]. The high cost of the low-band dye and environment-harmful PbS quantum dots, usually employed in the assembly of NIR-responded modified $TiO_2$, restricts the implement of this strategy. Moreover, the absorption in the NIR range of these available composites remains insufficiency. Therefore, it is desirable to develop alternative "green" $TiO_2$-based photocatalysts, which can be activated efficiently by NIR light to clean pollutants in the environment [20].

Recently, nanomaterials with upconversion (UC) emission property have attracted many attentions because of their potential applications in optical devices, bio-analysis, medical therapy, and photovoltaic cells [21,22]. UC emission is the nonlinear optical process which describes an UC material converting NIR light to visible or UV light by emitting higher-energy photons after absorbing lower-energy photons [23]. Among them, fluoride crystals have been regards as the outstanding UC matrixes owing to the low phonon energy and high chemical stability. Especially, high UC efficiency can be expected in rare earth ions ($RE^{3+}$) doped $NaYF_4$ crystals due to their unique optical properties arising from the intra 4f transitions [24–27]. So far, β-phase hexagonal phase $NaYF_4$:Yb, Er/Tm crystals have been demonstrated to be the best NIR-to-visible upconverting materials [28]. Hence, they might serve as an intermedium which, after absorbing NIR light, transfers energy to $TiO_2$ to generate strongly oxidative holes and reductive electrons. The following redox reaction of holes and electrons with $O_2$, $H_2O$ and $OH^-$ in solution may result in the generation of a series of reactive species, which are powerful nonselective oxidizing agents for environmental remediation.

In the last decade, $RE^{3+}$ doped nanoparticles employed as UC materials for the fabrication of advanced functional materials as strategy described above had been intensively explored [20–22]. The existing examples including $Er^{3+}$–$Yb^{3+}$ co-doped $TiO_2$ nanocrystals [29], $Er^{3+}$–$Yb^{3+}$ and $Er^{3+}$–$Y^{3+}$ co-doped $TiO_2$ films [30], $Er^{3+}$-doped $TiO_2$ nanocrystallites [31], $Er^{3+}$-$Yb^{3+}$-$Fe^{3+}$ tridoped $TiO_2$ nanopowder [32], $NaYF_4$:Yb, Tm/CdS photocatalyst [33], $TiO_2$/$NaYF_4$:Yb,Tm nanocomposites [34], $Er^{3+}$:$Y_3Al_5O_{12}$/$TiO_2$ nanomaterials [35,36], $YF_3$: $Yb^{3+}$, $Tm^{3+}$/$TiO_2$ core–shell nanoparticles [37], $Er^{3+}$-doped $Bi_2WO_6$ photocatalyst [38], $Y_2O_3$:$Yb^{3+}$,$Tm^{3+}$/$TiO_2$ nanocrystals [39], $Yb^{3+}$,$Tm^{3+}$/$TiO_2$ photocatalysis [40], $Er^{3+}$: $Y_3Al_5O_{12}$/$Bi_2WO_6$ [41], $Er^{3+}$-doped $Bi_2MoO_6$ [42], $Er^{3+}$–$TiO_2$ photocatalyst [43]. We are interested in the design and fabrication of $TiO_2$-based nanocomposite and the examination of activities of this novel photocatalyst in the NIR region. In this work, for the first time we propose the assembly of nanocomposites to be formed by β-phase hexagonal phase $NaYF_4$:$Yb^{3+}$,$Tm^{3+}$ rod as core and $TiO_2$ as shell, which present interesting high performance for organic pollutants degradation under NIR irradiation.

## 2. Experimental

### 2.1. Materials and reagents

$Y_2O_3$ (99.99%), $Yb_2O_3$ (99.99%), $Tm_2O_3$ (99.99%), ethylenediaminetetraacetic acid disodium salt (EDTA, AR), sodium fluoride (NaF, AR), ethanol (AR), hydrochloric acid (HCl, GR, 40%), titanium isopropoxide (TTIP, 98%), polyvinylpyrrolidone K-30 (PVP) were supplied by the Sinopharm Chemical Reagent Co., Ltd. (China). All

the chemicals were used as received without any further purification. Deionized (DI) water was used in all experiments.

### 2.2. Synthesis of β-$NaYF_4$:$Yb^{3+}$,$Tm^{3+}$ microcrystals

First, each $Re_2O_3$ ($Re^{3+}$ = $Y^{3+}$, $Yb^{3+}$ or $Tm^{3+}$) was separately dissolved in dilute HCl, then the solution was heated to evaporate water completely. The obtained rare earth metal trichloride ($ReCl_3$) was dissolved in DI water to prepare the stock solutions of $YCl_3$ (0.5 M), $YbCl_3$ (0.5 M) and $TmCl_3$ (0.01 M).

The hexagonal phase $NaYF_4$ microcrystals codoped with 25 wt% $Yb^{3+}$ and 0.6 wt% $Tm^{3+}$ (denoted β-$NaYF_4$:$Yb^{3+}$,$Tm^{3+}$) were synthesized by a modified hydrothermal method [44]. In a typical synthesis, 1.488 mL of $YCl_3$, 0.5 mL of $YbCl_3$ and 0.6 mL of $TmCl_3$ stock solutions were added into 15 mL of aqueous solution containing 2 mmol of EDTA and magnetically stirred for 1 h, forming a milky chelated Re–EDTA complex. Then 10 mL of NaF solution was added dropwise into the above mixture according to the $Re^{3+}$:$F^-$ molar ratio of 1:16. After stirring acutely for another 1 h, the mixture was transferred into a 50 mL Teflon-lined stainless steel autoclave and heated at 200 °C for 18 h, which followed by cooling down to room temperature (RT) slowly. The resulting precipitates were separated by centrifugation, washed with DI water and ethanol several times, and then dried in air at 70 °C for another 12 h. Finally, the product was annealed at 400 °C for 90 min under nitrogen atmosphere to improve the crystallinity of the UC materials.

### 2.3. Synthesis of β-$NaYF_4$:$Yb^{3+}$,$Tm^{3+}$@$TiO_2$ core-shell microcrystals

The β-$NaYF_4$:$Yb^{3+}$,$Tm^{3+}$@$TiO_2$ core–shell microcrystals were prepared by hydrolysis of TTIP with PVP as the coupling agent based on Qin's work, with modifications [37]. In a typical procedure, 50 mg of the β-$NaYF_4$:$Yb^{3+}$,$Tm^{3+}$ microcrystals were dispersed in 100 mL of ethanol in a 250 mL iodine flask by ultrasonic treatment for 30 min, then 2 g PVP was added into the above solution and stirring acutely for 1 h. After that, another solution including TTIP (5 mL) in ethanol (20 mL) was added dropwise into the iodine flask with vigorous stirring and then lasting for overnight. The resulting mixture was recovered by filtration, rinsed by ethanol and DI water several times, and dried in air at 70 °C for 12 h. Finally, the above product was calcined at 400 °C in nitrogen atmosphere for 90 min, resulting in β-$NaYF_4$:$Yb^{3+}$,$Tm^{3+}$@$TiO_2$ core-shell microcrystals.

### 2.4. Detection of photogenerated ·OH radicals [45,46]

Terephthalic acid (TP, $4 \times 10^{-4}$ M) was dissolved in NaOH ($2 \times 10^{-3}$ M) solution. In a typical process, 10 mg of β-$NaYF_4$:$Yb^{3+}$,$Tm^{3+}$@$TiO_2$ was mixed with 5 mL of TP solution. Then the mixture was irradiated with a NIR laser (λ = 980 nm). At every 30 min, 0.8 mL of the suspensions were sampled and centrifuged. Then 0.6 mL of the solution was diluted for the photoluminescence measurement. The hydroxylterephthalate anion formed was measured by fluorescence analysis with an excitation wavelength of 313 nm. In the contrast experiments, pure P25 and β-$NaYF_4$:$Yb^{3+}$,$Tm^{3+}$ were used and analyzed under identical conditions, respectively.

### 2.5. Photocatalytic activity measurements

The photocatalytic activities of the β-$NaYF_4$:$Yb^{3+}$,$Tm^{3+}$@$TiO_2$ core-shell microcrystals were evaluated by the decolorization of Methyl Orange (MO) in a homemade facility (Scheme 1). In detail, a 1 W 980 nm diode laser (Hi-tech Optoelectronics Co., Ltd.) was used as a NIR light source. 5 mg of photocatalyst was suspended
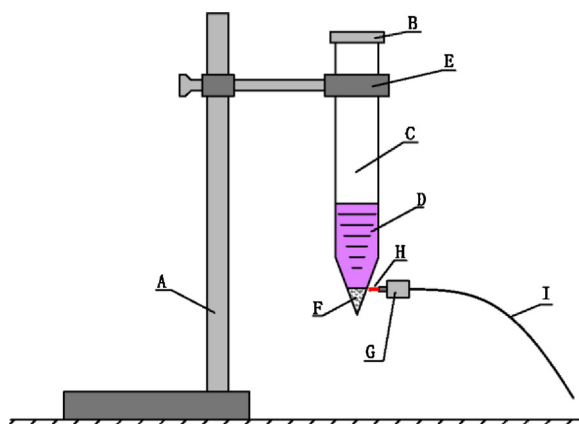
**Scheme 1.** Schematic illustration of the photo reaction system: (A) iron stand; (B) quartz plug; (C) 5 mL quartz cuvette; (D) pollutant; (E) brance; (F) catalyst; (G) the laser output; (H) 980 nm laser light; (I) optical fiber.

in a 0.5 mL of MO aqueous solution (20 ppm). Prior to irradiation, the suspension was kept in the dark for 12 h to establish an adsorption/desorption equilibrium between the photocatalyst and MO. Then the mixture was first irradiated with the NIR laser ($\lambda = 980 \pm 10$ nm, power = 1 W, fiber diameter = 100 $\mu$m). At given intervals, 0.3 mL of supernatant from MO aqueous solution was taken out and placed in the UV–vis spectrophotometer for analysis, and then put back after the measurement was done. The photocatalytic activity had also been demonstrated by using Methylene Blue (MB, 15 ppm) and Rhodamine B (RhB, 10 ppm) as probe, respectively. And the conditions are same as that used in the degradation of MO. The reactor was sealed when it worked and the system was set up in a dark box.

In the durability test of the $\beta$-NaYF$_4$:Yb$^{3+}$,Tm$^{3+}$@TiO$_2$ catalyst in the decolorization of MO under NIR light, four consecutive cycles were tested. The used catalyst was recovered by washing with DI water and ethanol. A new batch of dye solution then was added into the reactor with the recovered catalysts. The reaction was carried out using the same procedure as described above to check the catalyst stability. The percentage of decolorization was reported as $C/C_0$, in which $C$ is the absorbance of pollutants at each irradiated time interval of the main peak of the absorption spectrum, and $C_0$ is the absorbance of the initial concentration when the adsorption/desorption equilibrium is reached.

### 2.6. Characterization

The crystal structures of the obtained samples were determined at RT via powder X-ray diffraction using the Cu $K\alpha$ radiation (XRD, X' Pert Pro, PANalytical, Holand, 40 kV, 40 mA, $\lambda = 1.540598$ Å). Diffraction pattern were recorded between 10 and 80° with a step width of 0.02° s$^{-1}$. The morphology and structure of the samples were examined by a Hitachi Model S-4800 field-emission scanning electron microscope (FESEM) system. A thin film of gold was sprayed on the sample before the characterization. Analysis using a SEM system equipped for energy-dispersive X-ray (EDX) spectroscopy was performed to determine the composition of the samples. Transmission electron microscopy (TEM) measurements were carried out on a FEI Tecnai G20 operated at an acceleration voltage of 200 kV. All samples were first dispersed in ethanol and then collected using copper grids covered with carbon films for measurements. The photoluminescence spectra were recorded at RT using a fluorescence spectrometer (Hitachi F-4600) equipped with a R3788 photo counting photomultiplier tube (PMT), in conjunction with a commercial 980 diode laser. The spectra for all samples were recorded from solid samples immobilized on a quartz

glass slide with a small groove. All samples were measured under the same conditions (2.5 nm for spectral resolution, 250 V for PMT voltage and 1 W for the output power), except some that would be noted out. The temporal properties were studied under the OPO-LETTE II 355 Nd:YAG pumped OPO laser sub-system. The input power of the tunable OPO laser is <850 W, with a pulse band width of 4–7 cm$^{-1}$ and the pulse repetition rate of 20 Hz. The absorption spectra of various liquid samples were measured by Shimadzu UV-2450 UV–vis spectrophotometer. The absorption spectra of $\beta$-NaYF$_4$:Yb$^{3+}$,Tm$^{3+}$ and $\beta$-NaYF$_4$:Yb$^{3+}$,Tm$^{3+}$@TiO$_2$ were measured under the diffuse reflection mode using a Shimadzu UV-3600 UV–Vis–NIR spectrophotometer.

## 3. Results and discussion

The core–shell structure of $\beta$-NaYF$_4$:Yb$^{3+}$,Tm$^{3+}$@TiO$_2$, in which the surrounding TiO$_2$ shell encapsulating upconversion rare-earth fluoride microcrystals ($\beta$-NaYF$_4$:Yb$^{3+}$,Tm$^{3+}$), can be elaborately synthesized by a surfactant-assistant sol–gel coating process. As illustrated in Scheme 2(A), the uniform hexagonal NaYF$_4$:Yb$^{3+}$,Tm$^{3+}$ microcrystals synthesized by the modified hydrothermal method were uniformly dispersed in ethanol after ultrasonic treatment for 30 min, then these microcrystals were coated with a thin PVP layer to form PVP encapsulating $\beta$-NaYF$_4$:Yb$^{3+}$,Tm$^{3+}$ microcrystals (designated as $\beta$-NaYF$_4$:Yb$^{3+}$,Tm$^{3+}$@PVP). Amorphous TiO$_2$ shells surrounding the microcrystals were synthesized through the hydrolysis of TTIP with the aid of PVP as the coupling agent. The shell of PVP was removed after calcination and the NIR photocatalysis of $\beta$-NaYF$_4$:Yb$^{3+}$,Tm$^{3+}$@TiO$_2$ was finally fabricated, which demonstrated that NIR energy can be used as an activating source for TiO$_2$. As shown in Scheme 2(B), the composites can absorb NIR light after the NIR light penetrating the TiO$_2$ shell into the upconversion microcrystals core, followed by emitting UV light. UV light can excite TiO$_2$ to generate strongly oxidative holes (h$^+$) and reductive electrons (e$^-$), which subsequently induce powerful nonselective oxidizing agents, such as OH$^\bullet$ radical, for environmental remediation.

### 3.1. Structure and morphology characterizations

The size and morphology of the obtained materials were firstly examined by SEM. Fig. 1a displays a typical SEM image of the pure $\beta$-NaYF$_4$:Yb$^{3+}$,Tm$^{3+}$ microcrystals. The microcrystals are of a length roughly equal to 12 $\mu$m and diameter of 3.5 $\mu$m. The FESEM images show that the section surfaces of $\beta$-NaYF$_4$:Yb$^{3+}$,Tm$^{3+}$ microcrystals are hexagonal (Fig. 1b–f). As shown in the magnified SEM images (Fig. 1b and c), the surfaces of the microcrystals are rather smooth. However, after coating, the surfaces become rougher (Fig. 1d), implying that the microcrystals are successfully coated by TiO$_2$ layer. Fig. 1e and f present the enlarged views of the single rod-like sample of $\beta$-NaYF$_4$:Yb$^{3+}$,Tm$^{3+}$@TiO$_2$. Clearly, the $\beta$-NaYF$_4$:Yb$^{3+}$,Tm$^{3+}$ microcrystals are uniformly coated by TiO$_2$ shell. More detailed SEM images also confirm the unambiguous core–shell structure of the composites (Fig. S1). These results show that the $\beta$-NaYF$_4$:Yb$^{3+}$,Tm$^{3+}$@TiO$_2$ core–shell microcrystals have been successfully fabricated by this simple hydrothermal process.

For further detailed structure analysis, the characterization of the $\beta$-NaYF$_4$:Yb$^{3+}$,Tm$^{3+}$@TiO$_2$ core–shell microcrystals was carried out by TEM equipped with SAED. Fig. 1g clearly shows the TEM image of $\beta$-NaYF$_4$:Yb$^{3+}$,Tm$^{3+}$@TiO$_2$ core–shell structure, in which the core of $\beta$-NaYF$_4$:Yb$^{3+}$,Tm$^{3+}$ exhibits dark color. The clear-cut TiO$_2$ shell confirms that the upconversion microcrystals are uniformly coated by TiO$_2$ layer (Fig. S1h). The average thickness of TiO$_2$ shells is about 120 nm. A HRTEM and fast Fourier transform (FFT)
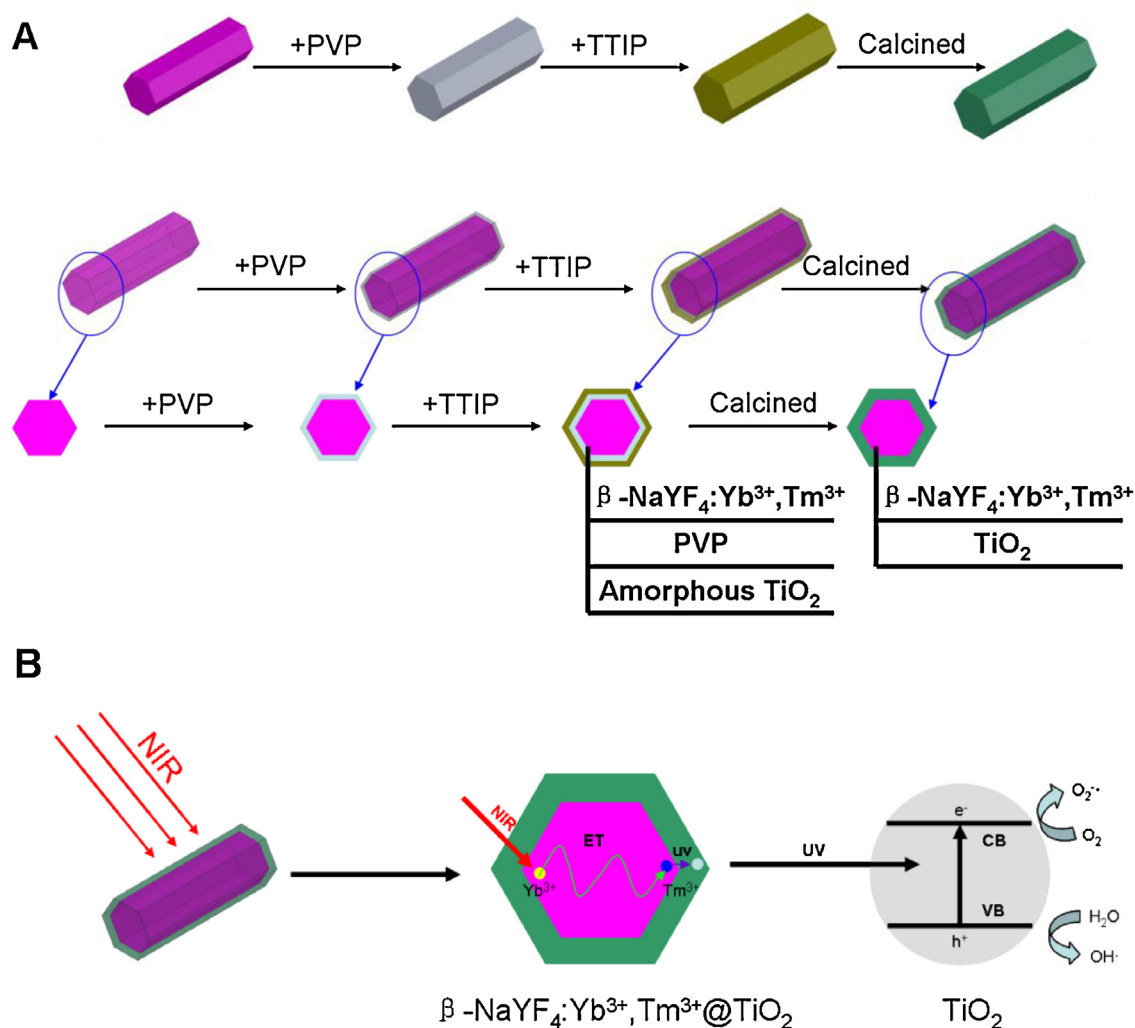
**Scheme 2.** (A) Strategy for the preparation of β-NaYF$_4$:Yb$^{3+}$,Tm$^{3+}$@TiO$_2$ core@shell microcrystals and (B) the mechanism of near-infrared-driven photocatalyst (ET: energy transfer).

images investigation provide insight into the fine microstructure and crystallinity of the as-synthesized samples. A representative HRTEM lattice image of the TiO$_2$ shell coated on the surface of the β-NaYF$_4$:Yb$^{3+}$,Tm$^{3+}$ is shown in Fig. 1i. The periodicity of the fine fringes is about 0.35 nm, which indicates the [1 0 1] plane of the anatase TiO$_2$ (JCPDS no. 01-073-1764). The corresponding FFT patterns taken from the TiO$_2$ shell show that the crystal plane is composed of [1 0 1] plane of the anatase phase (Fig. S1i, inset).

### 3.2. Composition studies

The crystal structures and the phase purity of the β-NaYF$_4$:Yb$^{3+}$,Tm$^{3+}$ and β-NaYF$_4$:Yb$^{3+}$,Tm$^{3+}$@TiO$_2$ were also examined by XRD. As shown in Fig. 2, the diffraction peaks' positions and intensities of the UC microcrystals could be readily indexed as hexagonal phase NaYF$_4$ crystal (JCPDS no. 16-0334) and no other impurity peaks were detected, which reveal that pure β-NaYF$_4$:Yb$^{3+}$,Tm$^{3+}$ has been fabricated. It can also be seen that the diffraction peaks of the samples are very sharp and strong, indicating that the samples with excellent crystallinity have been obtained at the high calcined temperature (400 °C), which is in good agreement with the results of TEM and SEM. High crystallinity is important requirement for efficient phosphors which is indirect benefit for photocatalysis [50]. The diffraction peaks of anatase TiO$_2$ (JCPDS no. 01-073-1764) were detected in the

samples of β-NaYF$_4$:Yb$^{3+}$,Tm$^{3+}$@TiO2. These XRD patterns clearly show that anatase TiO$_2$ and hexagonal phase NaYF$_4$ co-existed in these samples.

Scanning SEM-EDX was utilized to further verify the elemental composition of the as-synthesized samples. As shown in Fig. 3b and Fig. S2, EDX analysis of the samples reveals the presence of Ti$^{4+}$, O$^{2-}$, Yb$^{3+}$ and Tm$^{3+}$, suggesting that the Yb$^{3+}$ and Tm$^{3+}$ cations were codoped into the NaYF$_4$ lattice. It also suggests that TiO$_2$ exist in the samples. Fig. 3a shows a single rod-like composite and Fig. 3c–j show the corresponding elemental mappings for elements F, Na, Y, O, Ti, Yb and Tm, respectively. These images show that these elements were homogeneously distributed throughout the single rod-like composite, which further confirm that TiO$_2$ and hexagonal phase NaYF$_4$ co-exist in the samples. These results are in good agreement with the results of XRD, HRTEM and FTIR (Fig. S3).

### 3.3. Optical properties

The UV–vis–NIR absorption spectra of β-NaYF$_4$:Yb$^{3+}$,Tm$^{3+}$ and β-NaYF$_4$:Yb$^{3+}$,Tm$^{3+}$@TiO$_2$ are shown in Fig. 4a. It can be seen that β-NaYF$_4$:Yb$^{3+}$,Tm$^{3+}$@TiO$_2$ exhibit two strong absorption bands. The absorption band at UV region, which is located at about 387 nm, corresponds to the TiO$_2$ semiconductor band gap ($\leq$3.2 eV) [47]. The relatively wide absorption range at the NIR region, also presented in the spectra of β-NaYF$_4$:Yb$^{3+}$,Tm$^{3+}$, corresponds to the
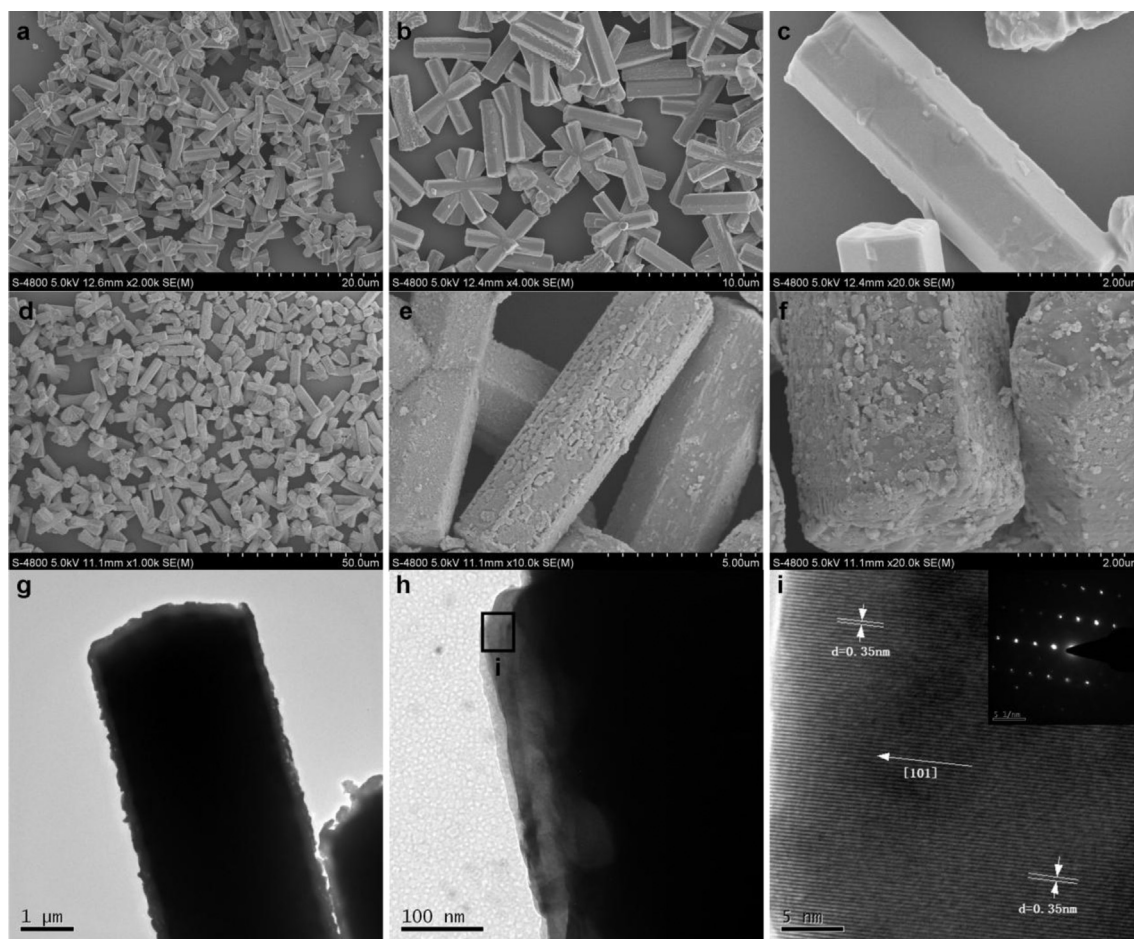
**Fig. 1.** SEM images of pure β-NaYF$_4$:Yb$^{3+}$,Tm$^{3+}$ (a–c) and β-NaYF$_4$:Yb$^{3+}$,Tm$^{3+}$@TiO$_2$ core@shell microcrystals (d–f); TEM images (g–i) of β-NaYF$_4$:Yb$^{3+}$,Tm$^{3+}$@TiO$_2$ core@shell microcrystals; (i) is the corresponding high-resolution TEM image from the areas outlined by the rectangle marked in (h). The inset of (i) is the SAED pattern of the corresponding TiO$_2$ single crystal in shell (i).

absorption of Yb$^{3+}$, which has a large absorption cross section from about 900 to 1100 nm [40]. After absorbing two or more NIR photons, β-NaYF$_4$:Yb$^{3+}$,Tm$^{3+}$ can emit visible and UV light, which indicates that the NIR can be indirectly utilized by TiO$_2$.

As shown in Fig. 4b, the β-NaYF$_4$:Yb$^{3+}$,Tm$^{3+}$ emits intense ultraviolet and blue upconversion luminescence under the excitation of a 980 nm laser. The UV emissions observed to be centered at about 265, 290, 345 and 362 nm, which can be attributed to the $^3P_2 \rightarrow {}^3H_6$, $^1I_6 \rightarrow {}^3H_6$, $^1I_6 \rightarrow {}^3F_4$, and $^1D_2 \rightarrow {}^3H_6$ transitions of Tm$^{3+}$ ions doped in β-NaYF$_4$ microcrystals, respectively [27,44,48–50]. The visible emissions from $^1D_2 \rightarrow {}^3F_4$, $^1G_4 \rightarrow {}^3H_6$, $^1D_2 \rightarrow {}^3H_5$, $^1D_2 \rightarrow {}^3H_4$, $^1G_4 \rightarrow {}^3F_4$ and $^3F_3 \rightarrow {}^3H_6$ transitions of Tm$^{3+}$ ions doped in β-NaYF$_4$ microcrystals, were detected at approximately 451, 475 (blue light), 510 (green light), 578, 647 and 692 nm (red light), respectively [48–50]. As a semiconductor with the bandgap of 3.2 eV, TiO$_2$ can absorb UV light ($\lambda < 380$ nm). It is very clear that the absorption band of TiO$_2$ overlaps very well with the UV emission peaks of UC particles. The spectral overlap indicates that the UC UV emission can be strongly quenched by being absorbed of TiO$_2$. The UC emissions spectra of the β-NaYF$_4$:Yb$^{3+}$,Tm$^{3+}$@TiO$_2$ composites were also recorded under the excitation of a 980 nm laser (Fig. 4b). As expected, the intensities of emission peaks are greatly reduced after being coated with TiO$_2$. It can be clearly observed from Fig. 4b that due to the absorption spectrum of TiO$_2$, the sample could hardly emit out 265, 290, 345 and 362 nm fluorescence under excited at 980 nm, and the intensities of blue emission peaks are also greatly reduced. The average thickness of the TiO$_2$ shells is about 120 nm (Fig. 1g), and the 980 nm NIR light can easily penetrate into the cores with the faded power density [50]. The faded power density could induce the emission intensities decrease slightly. Moreover, due to the existence of TiO$_2$ shells and the absorption of the emissions by the TiO$_2$ shells, the blue emission intensities will be decreased evidently with the poor ability of penetration and the UV emissions are quenched by being absorbed of TiO$_2$ shell (Fig. 4b).
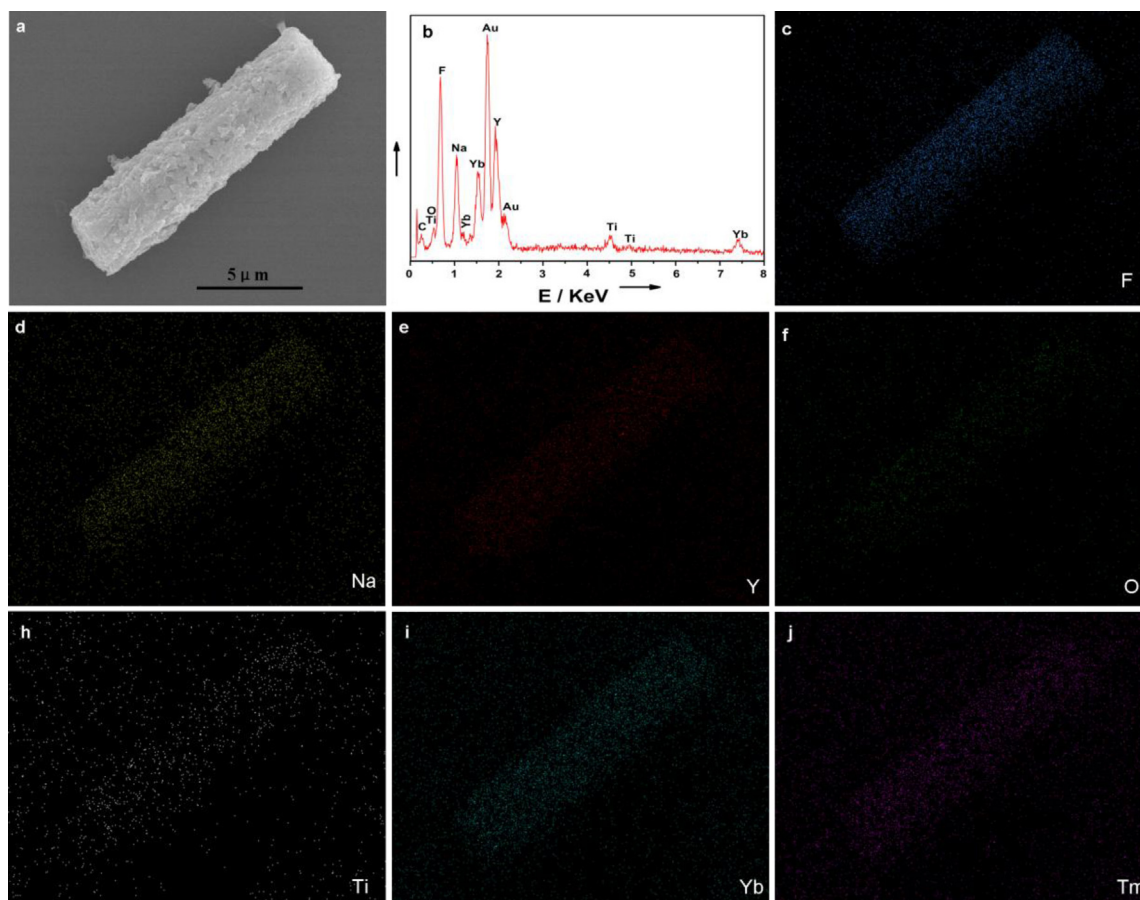


**Fig. 2.** The XRD patterns of β-NaYF$_4$:Yb$^{3+}$,Tm$^{3+}$ and β-NaYF$_4$:Yb$^{3+}$,Tm$^{3+}$@TiO$_2$.

**Fig. 3.** (a) Low-magnification SEM image of β-NaYF$_4$:Yb$^{3+}$,Tm$^{3+}$@TiO$_2$. (b) EDX spectrum of β-NaYF$_4$:Yb$^{3+}$,Tm$^{3+}$@TiO$_2$. (c–j) The corresponding scanning SEM elemental distribution mappings for F, Na, Y, O, Ti, Yb and Tm.

To rule out the effect of TiO$_2$ shells on the excitation power to β-NaYF$_4$:Yb$^{3+}$,Tm$^{3+}$, the UC emission spectra of Tm$^{3+}$ ions in β-NaYF$_4$:Yb$^{3+}$,Tm$^{3+}$ were also investigated under decreased excitation powers [37]. As shown in Fig. 4c, the profiles of the spectra remain unchanged as the excitation power decreases, while the β-NaYF$_4$:Yb$^{3+}$,Tm$^{3+}$@TiO$_2$ could hardly emit out 265, 290, 345 and 362 nm fluorescence (Fig. 4b). The quench of fluorescence in the UV range can be attributed to that the UV emissions have been absorbed by the TiO$_2$ shells. In order to further verify the effect of TiO$_2$ shells on the UC emission, the lifetimes of Tm$^{3+}$ ions in the β-NaYF$_4$:Yb$^{3+}$,Tm$^{3+}$ were detected under a 980 nm pulsed laser. The life time of the emission at 290, 345 and 362 nm for β-NaYF$_4$:Yb$^{3+}$,Tm$^{3+}$ and β-NaYF$_4$:Yb$^{3+}$,Tm$^{3+}$@TiO$_2$ were recorded (Fig. 4d–f). Each decay curve can be well fitted into a single exponential function $I(t) = I_0 \exp(-t/\tau)$, where $I_0$ is the initial emission intensity at $t = 0$, and $\tau$ is the lifetime [49]. The lifetimes of all radiated levels are listed in Table 1. As seen in Table 1, all the radiated lifetimes of Tm$^{3+}$ ions in the β-NaYF$_4$:Yb$^{3+}$,Tm$^{3+}$@TiO$_2$ are longer than those in the β-NaYF$_4$:Yb$^{3+}$,Tm$^{3+}$. This can be explained by that with a surface protection layer of the TiO$_2$ shell, surface quenching effect of the UC microparticles may be greatly decreased and longer lifetimes

of Tm$^{3+}$ ions in the β-NaYF$_4$:Yb$^{3+}$,Tm$^{3+}$@TiO$_2$ is resulted [51]. The less surface quenching centers in the NaYF$_4$:Yb$^{3+}$,Tm$^{3+}$@TiO$_2$ composite result in longer lifetimes of Tm$^{3+}$ ions in the β-NaYF$_4$:Yb$^{3+}$,Tm$^{3+}$@TiO$_2$ [48], and long lifetimes usually means high efficient UC luminescence [27]. It indicates that the core@shell structure indirectly contributes to the improved efficiency of the photocatalysis.

Hydroxyl radicals (OH$^\bullet$) are assumed to be the major species responsible for the degradation of pollutant molecules, which are generated on the surface of photocatalyst. Herein, a most used method, photoluminescence technique was applied to confirm the formation of OH$^\bullet$ radicals on the β-NaYF$_4$:Yb$^{3+}$,Tm$^{3+}$@TiO$_2$ under irradiation by 980 nm pulsed laser [45,46]. Terephthalic acid is used as a traditional fluorescent probe in the experiments [45,46]. As shown in Fig. 5a, the non-fluorescent terephthalic acid can convert into the highly fluorescent 2-hydroxyterephthalic acid with an emission peak at 420 nm under the excitation wavelength of 313 nm after trapping OH$^\bullet$ radicals. As expected, the fluorescence intensity increases nearly with irradiation time, which confirms the formation of OH$^\bullet$ radicals. For comparison, we carried out the control experiments involving pure P25 and β-NaYF$_4$:Yb$^{3+}$,Tm$^{3+}$, respectively. But OH$^\bullet$ radicals could not be generated, as shown in Fig. 5c. The detailed spectra are shown in Fig. S6. These results confirmed that OH$^\bullet$ radicals are generated on the surface of photocatalyst, which may be responsible for environmental remediation.

### 3.4. Photocatalytic properties

The NIR photocatalytic activities of samples were evaluated by the decoloration of dyes solution without investigating the

**Table 1**
The decay time constants of β-NaYF$_4$:Yb$^{3+}$,Tm$^{3+}$ ($\tau_1$) and β-NaYF$_4$:Yb$^{3+}$,Tm$^{3+}$@TiO$_2$ ($\tau_1$), respectively.

| $\lambda_{em}$ (nm) | 290 | 345 | 362 |
|---|---|---|---|
| $\tau_1$ (μs) | 137.54 | 135.38 | 191.55 |
| $\tau_2$ (μs) | 173.02 | 183.20 | 247.46 |
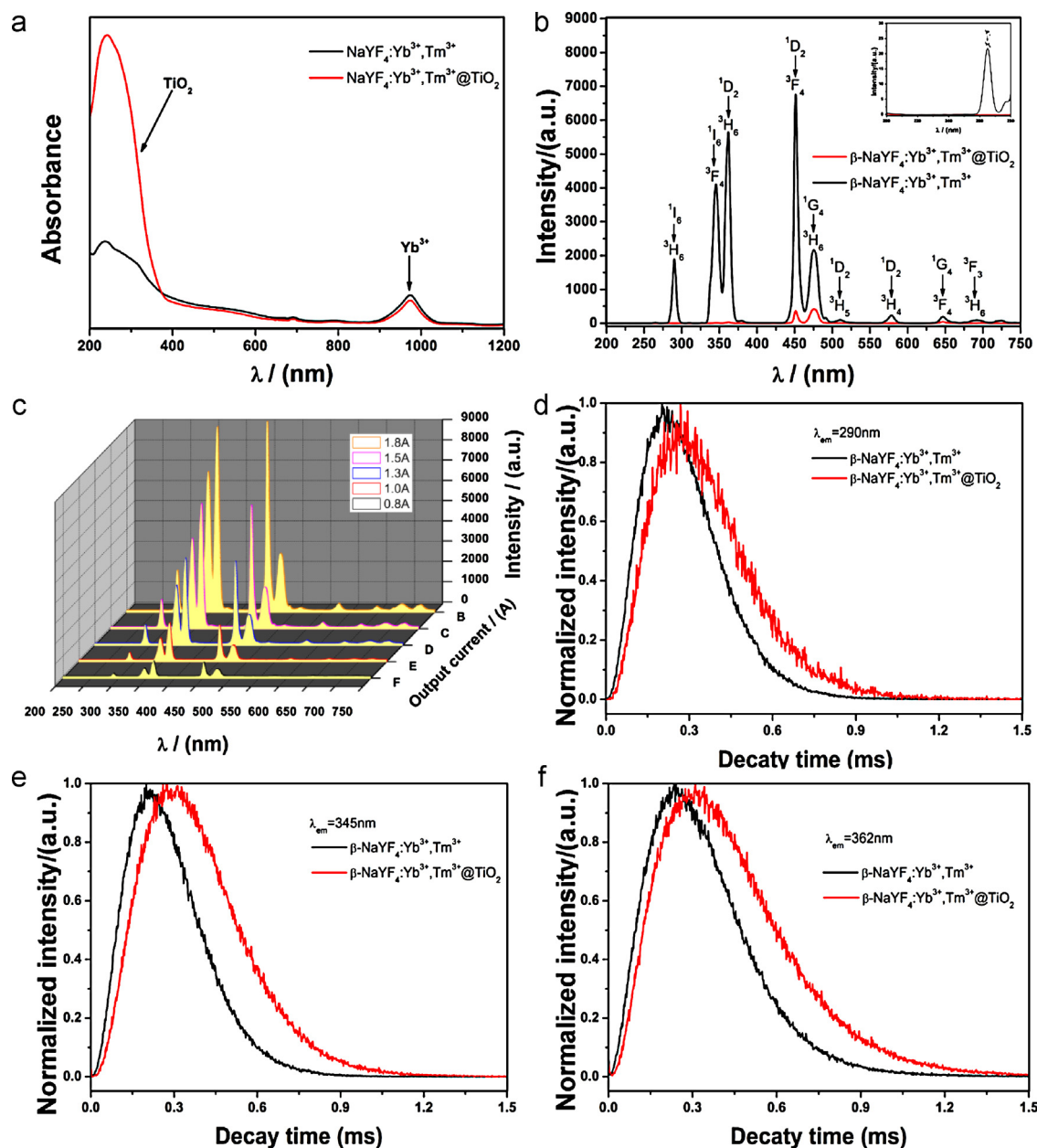
**Fig. 4.** (a) The UV–Vis–NIR absorption spectrum of the β-NaYF$_4$:Yb$^{3+}$,Tm$^{3+}$ and β-NaYF$_4$:Yb$^{3+}$,Tm$^{3+}$@TiO2. (b) UC emission spectra of β-NaYF$_4$:Yb$^{3+}$,Tm$^{3+}$ and β-NaYF$_4$:Yb$^{3+}$,Tm$^{3+}$@TiO$_2$ under 980 excitation; inset: the enlarge spectra ranging from 200 nm to 280 nm. (c) UC emission spectrum of β-NaYF$_4$:Yb$^{3+}$,Tm$^{3+}$ under different excitation powers. (d–f) Time-resolved fluorescence decay curves of Tm$^{3+}$ ($\lambda_{em}$ = 290 nm, $\lambda_{em}$ = 345 nm, $\lambda_{em}$ = 362 nm,) in the β-NaYF$_4$:Yb$^{3+}$,Tm$^{3+}$ and β-NaYF$_4$:Yb$^{3+}$,Tm$^{3+}$@TiO$_2$, respectively.

degradation intermediates in detail. Before irradiation, a dark adsorption test was carried out to estimate the adsorptivity of β-NaYF$_4$:Yb$^{3+}$,Tm$^{3+}$@TiO$_2$. Under irradiation by the 980 nm NIR laser, it can be seen from Fig. 6a that the β-NaYF$_4$:Yb$^{3+}$,Tm$^{3+}$@TiO$_2$ possesses the best photocatalytic activity to decolorize MB solution, and about 68.37% of MB is decolored in 24 h under our experimental conditions. As reference experiments, the photodegradation of MB with P25 or β-NaYF$_4$:Yb$^{3+}$,Tm$^{3+}$ or without NIR irradiation were tested, and no obvious degradation of MB was verified. It indicates that NIR light can effectively drive the β-NaYF$_4$:Yb$^{3+}$,Tm$^{3+}$@TiO$_2$ for photocatalysis. To further demonstrate the photoactivity, NIR driven photocatalytic degradation of MO and RhB have also been investigated as shown in Fig. 6b and c. All the experiments are at the same conditions for comparison. It can be shown that 69.34% of MO and 75.75% RhB are decolored in 24 h, respectively. Despite the

discrepant adsorptivity of β-NaYF$_4$:Yb$^{3+}$,Tm$^{3+}$@TiO$_2$ to dyes (Fig. 6d), all the results doubtless confirm that β-NaYF$_4$:Yb$^{3+}$,Tm$^{3+}$@TiO$_2$ is an effective photocatalyst for organic pollutant under irradiation by NIR light.

### 3.5. Mechanisms

The mechanism for the NIR-driven photocatalysis is shown in Fig. 7. The pump light only excites the Yb$^{3+}$ ions which result in populating the $^2F_{5/2}$ level. A Tm$^{3+}$ ion is excited to the $^3H_5$ level after the energy transferred (ET) from the excited Yb$^{3+}$, and then relaxes nonradiatively to the $^3F_4$ level. ET from another Yb$^{3+}$ ion to the Tm$^{3+}$ leads to the formation of the $^3F2$ level. Subsequently, the $^3F_2$ level of Tm$^{3+}$ relaxes to the $^3H_4$ level and then is excited to the $^1G_4$ level by ET from another excited Yb$^{3+}$ ions.
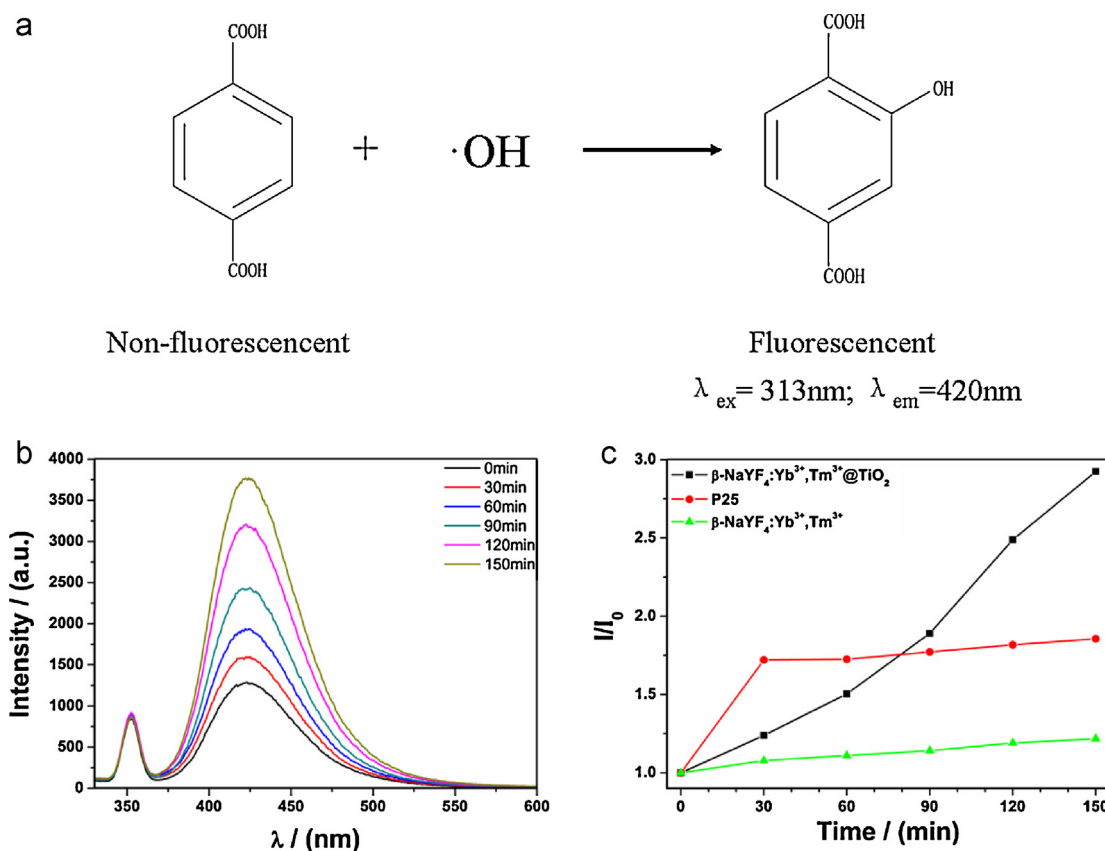
**Fig. 5.** (a) Formation of 2-hydroxyterphthalic acid as a result of the reaction between terephthalic acid and OH•. (b) Time-dependent fluorescence spectra observed during NIR illumination of β-NaYF$_4$:Yb$^{3+}$,Tm$^{3+}$@TiO$_2$ in terephthalic acid slution ($4 \times 10^{-4}$ M, excitation at 313 nm). (c) Fluorescence intensity of the emission peak at 420 nm as a function of NIR irradiation time.
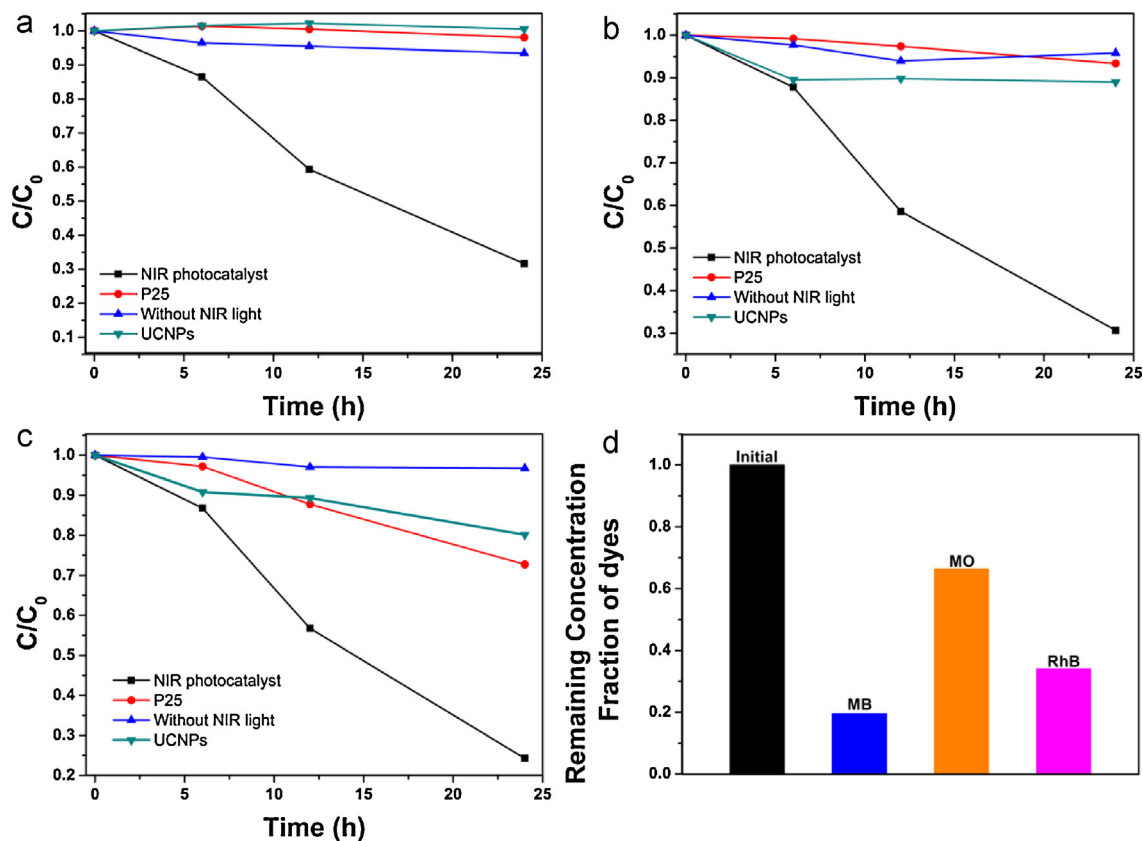


**Fig. 6.** Plot of dye concentration versus irradiation time for the photodegradation of MB (a), MO (b) and RhB (c) catalyzed by β-NaYF$_4$:Yb$^{3+}$,Tm$^{3+}$@TiO$_2$ NIR photocatalyst under 980 nm NIR light. Bar plot showing the remaining dyes in solution after reaching the adsorption equilibrium in the dark for 12 h (d).
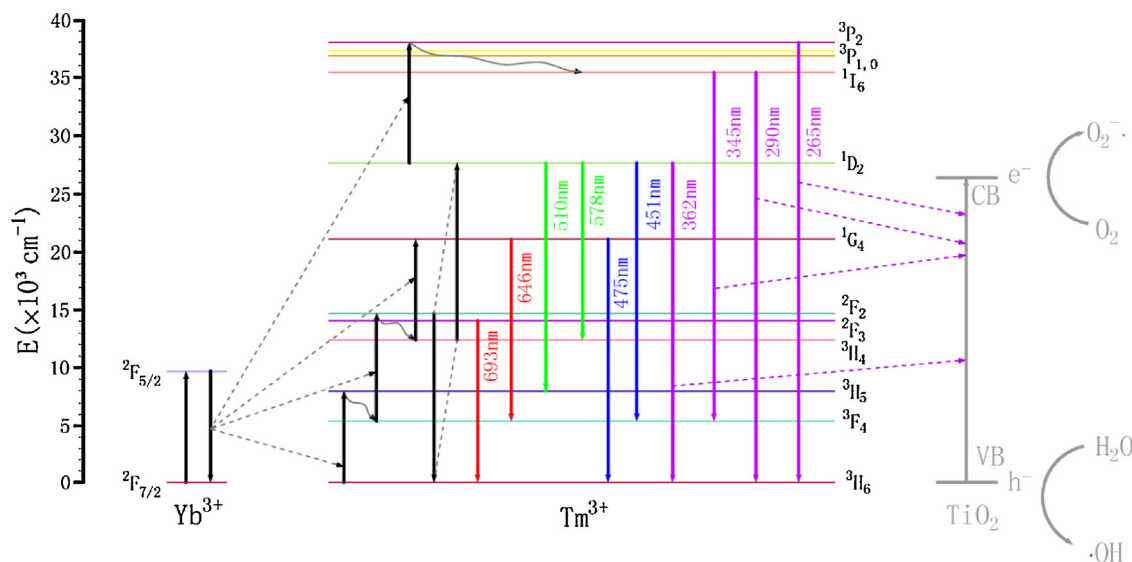
**Fig. 7.** Schematic energy-level diagrams of $Yb^{3+}$, $Tm^{3+}$ and the upconversion mechanism and the energy transfer mechanism from β-NaYF$_4$:$Yb^{3+}$,$Tm^{3+}$ to TiO$_2$ under 980 nm NIR irradiation.

The $^1D_2$ level of $Tm^{3+}$ cannot be populated by the fourth ET from $Yb^{3+}$ ions owing to the large energy mismatch (about 3500 cm$^{-1}$) between the $^1G_4$ and the $^1D_2$ levels. This intense ultraviolet emissions can be attributed to the efficient cross relaxation process $^3F_2$ (or $^3F_3$) + $^3H_4 \rightarrow {}^3H_6 + {}^1D_2$ between two $Tm^{3+}$ ions, which consequently results in the population of $^1D_2$ level. Some of the populated $^1D_2$ levels then make transitions to the $^1I_6$ and $^3P_2$ levels by another and further ET [48–50]. Then the excited $Tm^{3+}$ ions fall to the lower energy level. $^1G_z \rightarrow {}^3H_6$, $^1D_2 \rightarrow {}^3F_4$, $^1D_2 \rightarrow {}^3H_6$, $^1I_6 \rightarrow {}^3F_4$, $^1I_6 \rightarrow {}^3H_6$ and $^3P_2 \rightarrow {}^1I_6$ transitions cause the blue emissions at about 475 and 451 nm, and UV emissions at 362, 345, 290 and 265 nm, respectively [48–50]. The energy gap of TiO$_2$ is about 3.2 eV [47], hence ultraviolet light ($\lambda \leq 387$ nm) is necessary to activate TiO$_2$ for photocatalytic reactions. So the TiO$_2$ on the shells can absorb the UV emissions from β-NaYF$_4$:$Yb^{3+}$,$Tm^{3+}$ and induce the formation of photoelectrons (e$^-$) and holes (h$^+$), where e$^-$ is a powerful oxidant and h$^+$ is a strong reductant. The redox reactions of e$^-$ or h$^+$ with O$_2$, H$_2$O and OH$^-$ also result in the generation of very reactive species such as superoxide (O$_2^{-\bullet}$) and hydroxyl radicals (OH$^\bullet$). Those reactive oxygen species are known to be nonselective oxidizing agents for many organic pollutants.

### 3.6. Photochemical stability and recyclability

To evaluate the repeatability of NIR-driven photocatalyst under 980 NIR light irradiation, the recycled experiments for decoloration of MO solution for 24 h of 980 NIR light irradiation were carried out four consecutive cycles. After each 24 h of photocatalytic reaction, the fresh MO solution (20 ppm, 0.5 mL) was injected and the separated photocatalysts, which had been washed with distilled water and ethanol for several times, were added into the 5 mL quartz cuvette in order to keep the conditions of all the recycled experiments same (5 mg per run). As shown in Fig. 8, about 69.34% of MO could be decolored when the NIR-driven photocatalyst is used for the first run. After the first run, there is no significant decrease of photocatalytic activity and about 45% of MO is decolored in the forth cycle, which indicated the good repeatability of the NIT-driven photocatalytic activity of β-NaYF$_4$:$Yb^{3+}$,$Tm^{3+}$@TiO$_2$. The slightly deactivation of β-NaYF$_4$:$Yb^{3+}$,$Tm^{3+}$@TiO$_2$ probably results from several factors. But we believe most important reason is that the TiO$_2$ shells may be slightly damaged due to mechanical operation when photocatalysts were centrifuged and separated. It could
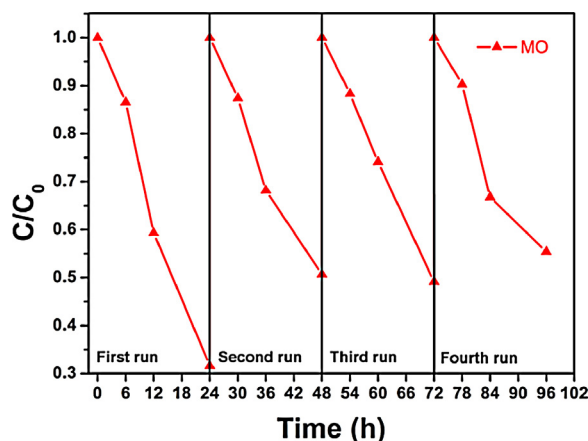


**Fig. 8.** Cycling runs in the decoloration of Methyl Orange in the presence on β-NaYF$_4$:$Yb^{3+}$,$Tm^{3+}$@ TiO$_2$ under 980 NIR irradiation; addition of methyl orange (20 ppm, 0.5 mL), β-NaYF$_4$:$Yb^{3+}$,$Tm^{3+}$@TiO$_2$ (10 g/L, per run).

cause loss of the TiO$_2$ particle, so the photocatalyst activity will be affected.

## 4. Conclusions

In summary, we have successfully fabricated β-NaYF$_4$:$Yb^{3+}$,$Tm^{3+}$@TiO$_2$ core@shell microcrystals as an advanced NIR-driven photocatalyst, evaluated by decoloration of dyes (MB, MO and RhB). The morphology and composition of the advanced NIR-driven photocatalyst were investigated thoroughly. The energy transfer from β-NaYF$_4$:$Yb^{3+}$,$Tm^{3+}$ to TiO$_2$ was confirmed. Moreover the NIR-driven photocatalyst showed good stability for photocatalytic decoloration of MO in the recycled tests. This study suggests a promising system to utilizing the NIR energy of sunlight for photochemical and photoelectrical applications based on TiO$_2$, which will contribute to the utilization of solar energy in the future.

## Appendix A. Supplementary data

Supplementary data associated with this article can be found, in the online version, at http://dx.doi.org/10.1016/j.apcatb. 2013.05.062.

## References

[1] Z.Y. Zhao, J. Zuo, L.L. Fan, G. Zillante, Renewable Energy 36 (2011) 24–30.
[2] L. Liu, S. Cheng, J. Li, Y. Huang, Energy Sources Part A: Recovery Utilization and Environmental Effects 29 (2007) 1069–1080.
[3] I.K. Konstantinou, T.A. Albanis, Applied Catalysis B: Environmental 49 (2004) 1–14.
[4] M. Ni, M.K.H. Leung, D.Y.C. Leung, K. Sumathy, Renewable & Sustainable Energy Reviews 11 (2007) 401–425.
[5] H. Tong, S. Ouyang, Y. Bi, N. Umezawa, M. Oshikiri, J. Ye, Advanced Materials 24 (2012) 229–251.
[6] S.G. Kumar, L.G. Devi, Journal of Physical Chemistry A 115 (2011) 13211–13241.
[7] M. Pelaez, N.T. Nolan, S.C. Pillai, M.K. Seery, P. Falaras, A.G. Kontos, P.S.M. Dunlop, J.W.J. Hamilton, J.A. Byrne, K. O'Shea, M.H. Entezari, D.D. Dionysious, Applied Catalysis B: Environmental 125 (2012) 331–349.
[8] I.M. Freedberg, A.Z. Eisen, S.I. Katz, K. Wolff, L.A. Goldsmith, K.F. Austen, T.B. Fitzpatrick, Fitzpatrick's Dermatology in General Medicine, McGraw-Hill, New York, 1999, pp. 220–229 (September).
[9] R. Asahi, T. Morikawa, T. Ohwaki, K. Aoki, Y. Taga, Science 293 (2001) 269–271.
[10] S. Sakthivel, H. Kisch, Angewandte Chemie International Edition 115 (2003) 5057–5060, Angew. Chem. Int. Ed. 42 (2003) 4908–4911.
[11] S.U.M. Khan, M. Al-Shahry, W.B. Ingler, Science 297 (2002) 2243–2245.
[12] A. Emeline, V. Kuznetsov, V. Rybchuk, N. Serpone, International Journal of Photoenergy 2008 (2008) 1–19.
[13] X. Chen, L. Liu, P.Y. Yu, S.S. Mao, Science 331 (2011) 746–750.
[14] M. Paulose, K. Shankar, O.K. Varghese, G.K. Mor, C.A. Grimes, Journal of Physics D: Applied Physics 39 (2006) 2498–2503.
[15] C. Ratanatawanate, A. Bui, K. Vu, K.J. Balkus Jr., Journal of Physical Chemistry C 115 (2011) 6175–6180.
[16] S.A. Mcdonald, G. Konstantatos, S. Zhang, P.W. Cyr, E.J.D. Klem, L. Levina, E.H. Sargent, Nature Materials 4 (2005) 138–142.
[17] S.L. Li, K.J. Jiang, K.F. Shao, L.M. Yang, Chemical Communications 26 (2006) 2792–2794.
[18] J.J. Cid, J.H. Yum, S.R. Jang, M.K. Nazeeruddin, E.M. Ferrero, E. Palomares, J. Ko, M. Grätzel, T. Torres, Angewandte Chemie International Edition 46 (2007) 8358–8362.
[19] G.B. Shan, G.P. Demopoulos, Advanced Materials 22 (2010) 4373–4377.
[20] A.S. Weber, A.M. Grady, R.T. Koodali, Catalysis Science & Technology 2 (2012) 683–693.
[21] F. Auzel, Chemical Reviews 104 (2004) 139–173.
[22] F. Wang, X.G. Liu, Chemical Society Reviews 38 (2009) 976–989.
[23] N. Bloembergen, Physical Review Letters 2 (1959) 84–85.
[24] J.F. Suyver, J. Grimm, K.W. Krämer, H.U. Güdel, Journal of Luminescence 114 (2005) 53–59.
[25] F. Vetrone, J. Boyer, J. Capobianco, A. Speghini, M. Bettinelli, Journal of Applied Physics 96 (2004) 661–667.
[26] G.Y. Chen, T.Y. Ohulchanskyy, R. Kumar, H. Agren, P.N. Prasad, ACS Nano 4 (2010) 3163–3168.
[27] T. Jiang, W.P. Qin, W.H. Di, R.Y. Yang, D.M. Liu, X.S. Zhai, G.S. Qin, CrystEngComm 14 (2012) 2302–2307.
[28] S. Heer, K. Kompe, H.U. Güdel, M. Haase, Advanced Materials 16 (2004) 2102–2104.
[29] Q.K. Shang, H. Yu, X.G. Kong, H.D. Wang, X. Wang, Y.J. Sun, Y.L. Zang, Q.H. Zeng, Journal of Luminescence 128 (2008) 1211–1216.
[30] S.Y. Chen, C.C. Ting, W.F. Hsieh, Thin Solid Films 434 (2003) 171–177.
[31] A. Patra, C.S. Friend, R.P. Kapoor, N. Prasad, Chemistry of Materials 15 (2003) 3650–3655.
[32] W.L. Wang, Q.K. Shang, W. Zheng, H. Yu, X.J. Feng, Z.D. Wang, Y.B. Zhang, G.Q. Li, Journal of Physical Chemistry C 114 (2010) 13663–13669.
[33] C. Li, F. Wang, J. Zhu, J.C. Yu, Applied Catalysis B: Environmental 100 (2010) 433–439.
[34] Q.C. Xu, Y. Zhang, M.J. Tan, Y. Liu, S.J. Yuan, C. Choong, N.S. Tan, T.T.Y. Tan, Advanced Healthcare Materials 1 (2012) 470–474.
[35] J. Wang, R. Li, Z. Zhang, W. Sun, R. Xu, Y. Xie, Z. Xing, X. Zhang, Applied Catalysis A: General 334 (2008) 227–233.
[36] G. Feng, S. Liu, Z. Xiu, Y. Zhang, J. Yu, Y. Chen, P. Wang, X. Yu, Journal of Physical Chemistry C 112 (2008) 13692–13699.
[37] W.P. Qin, D.S. Zhang, D. Zhao, L.L. Wang, K.Z. Zheng, Chemical Communications 46 (2010) 2304–2306.
[38] Z. Zhang, W. Wang, W. Yin, M. Shang, L. Wang, S. Sun, Applied Catalysis B: Environmental 101 (2010) 68–73.
[39] T. Li, S. Liu, H. Zhang, E. Wang, L. Song, P. Wang, Journal of Materials Science 46 (2011) 2882–2886.
[40] Z.X. Li, F.B. Shi, T. Zhang, H.S. Wu, L.D. Sun, C.H. Yan, Chemical Communications 47 (2011) 8109–8111.
[41] Z. Zhang, W. Wang, J. Xu, M. Shang, J. Ren, S. Sun, Catalysis Communications 13 (2011) 31–34.
[42] T. Zhou, J. Hu, J. Li, Applied Catalysis B: Environmental 110 (2011) 221–230.
[43] S. Obregón, G. Colón, Chemical Communications 48 (2012) 7865–7867.
[44] G.F. Wang, W.P. Qin, L.L. Wang, G.D. Wei, P.F. Zhu, R. Kim, Optics Express 16 (2008) 11907–11914.
[45] K.I. Ishibashi, A. Fujishima, T. Watanabe, K. Hashimotoa, Journal of Photochemistry and Photobiology A: Chemistry 134 (2000) 139–142.
[46] K.I. Ishibashi, A. Fujishima, T. Watanabe, K. Hashimotoa, Electrochemistry Communications 2 (2000) 207–710.
[47] D. Mitoraj, H. Kisch, Angewandte Chemie International Edition 47 (2008) 9975–9978.
[48] F. Shi, J.S. Wang, D.S. Zhang, G.S. Qin, W.P. Qin, Journal of Materials Chemistry 21 (2011) 13413–13421.
[49] N. Liu, W.P. Qin, G.S. Qin, T. Jiang, D. Zhao, Chemical Communications 47 (2011) 7671–7673.
[50] F. Shi, J.S. Wang, X.S. Zhai, D. Zhao, W.P. Qin, CrystEngComm 13 (2011) 3782–3787.
[51] F. Wang, J. Liu, X.G. Wang, Angewandte Chemie International Edition 49 (2010) 7456–7460.